



Article

Spatio-Temporal Mapping of Multi-Satellite Observed Column Atmospheric CO₂ Using Precision-Weighted Kriging Method

Zhonghua He ^{1,2}, Liping Lei ^{2,*}, Yuhui Zhang ¹, Mengya Sheng ², Changjiang Wu ², Liang Li ³, Zhao-Cheng Zeng ⁴  and Lisa R. Welp ⁵ 

¹ Zhejiang Climate Center, Hangzhou 310017, China; hezhzh@radi.ac.cn (Z.H.); zhyuh@mail3.sysu.edu.cn (Y.Z.)

² Key Laboratory of Digital Earth Science, Institute of Remote Sensing and Digital Earth, Chinese Academy of Sciences, Beijing 100094, China; shengmy@radi.ac.cn (M.S.); wucj@radi.ac.cn (C.W.)

³ The Third Engineering of Surveying and Mapping Academy in Sichuan Province, Chengdu 610500, China; heling@whu.edu.cn

⁴ Division of Geological and Planetary Sciences, California Institute of Technology, Pasadena, CA 91125, USA; zcz@gps.caltech.edu

⁵ Department of Earth, Atmospheric, and Planetary Sciences, Purdue University, West Lafayette, IN 47907-2051, USA; lwelp@purdue.edu

* Correspondence: leilp@radi.ac.cn

Received: 20 December 2019; Accepted: 6 February 2020; Published: 9 February 2020



Abstract: Column-averaged dry air mole fraction of atmospheric CO₂ (XCO₂), obtained by multiple satellite observations since 2003 such as ENVISAT/SCIAMACHY, GOSAT, and OCO-2 satellite, is valuable for understanding the spatio-temporal variations of atmospheric CO₂ concentrations which are related to carbon uptake and emissions. In order to construct long-term spatio-temporal continuous XCO₂ from multiple satellites with different temporal and spatial periods of observations, we developed a precision-weighted spatio-temporal kriging method for integrating and mapping multi-satellite observed XCO₂. The approach integrated XCO₂ from different sensors considering differences in vertical sensitivity, overpass time, the field of view, repeat cycle and measurement precision. We produced globally mapped XCO₂ (GM-XCO₂) with spatial/temporal resolution of 1 × 1 degree every eight days from 2003 to 2016 with corresponding data precision and interpolation uncertainty in each grid. The predicted GM-XCO₂ precision improved in most grids compared with conventional spatio-temporal kriging results, especially during the satellites overlapping period (0.3–0.5 ppm). The method showed good reliability with R² of 0.97 from cross-validation. GM-XCO₂ showed good accuracy with a standard deviation of bias from total carbon column observing network (TCCON) measurements of 1.05 ppm. This method has potential applications for integrating and mapping XCO₂ or other similar datasets observed from multiple satellite sensors. The resulting GM-XCO₂ product may be also used in different carbon cycle research applications with different precision requirements.

Keywords: XCO₂; multi-satellites; precision weighting; spatio-temporal kriging; mapping

1. Introduction

Spatio-temporal variation of atmospheric CO₂ concentration reflects the balance between anthropogenic carbon emissions and terrestrial and oceanic carbon uptake or emissions [1]. Increased fossil fuel emissions after the start of the Industrial Revolution contribute to the continuous growth of atmospheric CO₂ concentrations [2] from 277 parts per million (ppm) in 1750 [3] to 407.4 ± 0.1 ppm in 2018 [4]. The growth rate of CO₂ concentrations in the atmosphere is smaller than the rate

of CO₂ emitted by human activities because nearly 45% of the emissions are absorbed by oceans and the terrestrial biosphere each year [5]. The seasonal variations of terrestrial carbon uptake and emission contribute most to the seasonal cycle in atmospheric CO₂ [6], which varies spatially due to non-uniform land-biosphere CO₂ exchange [7]. In addition, there is spatial-temporal variability of atmospheric CO₂ concentrations that can be used to study changes in regional land biosphere net CO₂ fluxes, for example, seasonal cycle amplitude increase [8,9] and regional effects of extreme weather patterns like droughts [10,11]. Atmospheric CO₂ concentrations have also been used for carbon flux or to estimate carbon uptake/emission changes using atmospheric inversion models [12,13] and a data-driven method [14]. The spatio-temporal variability of CO₂ and related carbon sources/sinks distribution are still not fully understood [15,16]. A long time series of comparable global CO₂ concentration datasets has the potential to improve our understanding of land-biosphere interactions and our ability to evaluate trends in regional terrestrial CO₂ absorption capacity.

There are several methods to measure atmospheric CO₂ concentrations, including surface measurements and satellite observations and approaches to estimate concentrations from model simulations. A network of surface CO₂ monitoring station observations has been organized into the popular GLOBALVIEW-CO₂ product and provides in situ measurements but is limited by station sparseness and the inherent spatial inhomogeneity of the surface atmosphere. Model simulations can provide continuous maps of CO₂ using estimated surface fluxes and atmospheric mixing transport in addition to the previously noted sparse validation stations [17]. Satellite observations of atmospheric CO₂ have the advantage of global coverage and high measurement density and can complement the surface network to advance our understandings of the carbon cycle and its changes [18,19]. With the development of remote sensing technology, there are several satellites used for atmospheric CO₂ concentration observations [20,21]. Leveraging all available XCO₂ datasets to construct a long time series, continuous, and comparable global CO₂ concentrations would be useful.

Satellite-observed column-averaged dry air mole fraction of CO₂ (XCO₂) have been widely used for carbon cycle studies, including CO₂ enhancement detection induced by anthropogenic emissions [22,23], constraining model simulations of carbon fluxes [24,25], investigating carbon cycle responses to weather extremes [11,26], and improving understanding of vegetation uptake [27]. Satellites measuring XCO₂ are the SCanning Imaging Absorption spectroMeter for Atmospheric CHartographY (SCIAMACHY) onboard the Environmental Satellite (ENVISAT) [28], Greenhouse Gases Observing Satellite (GOSAT) [29], and Orbiting Carbon Observatory-2 (OCO-2) [30]. They observe XCO₂ but with different spatial/temporal resolution, prior vertical profile estimates, local overpass time, data precision, and observing gaps. As a result, there is an opportunity to generate a long time series of global XCO₂ dataset starting from 2003 using XCO₂ retrievals from these satellites with careful integration and gap-filling.

Gap-filling satellite-observed XCO₂ has been investigated in several studies from different perspectives [31–33]. Geostatistical approaches, especially kriging, were widely used for GOSAT observed XCO₂ Level 3 product production [17,34,35]. Spatial-only geostatistical methods do not take into account the temporal correlation structure of CO₂ data [19], which may provide extra information. In order to make full use of spatio-temporal correlation of atmospheric CO₂, a new spatio-temporal kriging method was developed for the global mapping of XCO₂ [19,36]. Because these methods were previously used for observations from a single satellite, measurement error could be assumed to be uniform and not interfere with the kriging approach. In order to produce high spatio-temporal resolution and a long time series of XCO₂ from multiple satellite observations, the precision of different datasets should be considered in this geostatistical method.

In this study, to create the longest possible time series of XCO₂ and leverage multiple measurements to improve precision when possible, we developed a precision-weighted spatio-temporal kriging method for gap filling of integrated XCO₂ from multiple satellite observations. Datasets used in this study and data preprocessing are described in Section 2. XCO₂ integration methods and global mapping can be found in Section 3. Results of global mapped XCO₂ and its validation are shown in

Section 4 and data quality considerations are discussed in Section 5. Finally, conclusions are presented in Section 6.

2. Dataset

In this study, we collected atmospheric CO₂ concentration datasets from multiple satellite-observations to produce a long time series of spatio-temporal continuous XCO₂ from satellite observations, which was then evaluated by XCO₂ from surface measurements and model simulations.

2.1. XCO₂ from Multi-Satellite Observations

Atmospheric CO₂ concentrations used here were the released Level 2 products that contain the full-physics retrievals of column-averaged CO₂ in units of dry air mole fraction (XCO₂). Satellite observations of XCO₂ used here are from ENVISAT/SCIAMACHY, GOSAT, and OCO-2, which span from 2003 to 2016. XCO₂ from SCIAMACHY onboard the European ENVISAT are obtained by the full-physics based Bremen Optimal Estimation–DOAS (BESD) algorithm (v02.01.01) [37], which span from January 2003 to March 2012 with a spatial/temporal resolution of 30x60 km every 35 days. XCO₂ from GOSAT is produced by the algorithm of the Atmospheric CO₂ Observations from Space (ACOS) team (v7.3 lite) [38], which span from June 2009 to May 2016 with spatial/temporal resolution of a diameter of 10.5 km every three days. XCO₂ from OCO-2 is produced by the ACOS team (r9 lite) [39], which span from September 2014 to December 2016 with spatial/temporal resolution of 2.25 × 1.25 km every 16 days. Data quality was maximized by filtering XCO₂ product by screening criteria specified by the corresponding user guides. Specifications of the three satellites that observed XCO₂ are shown in Table 1. These satellites follow different orbits and have different gaps as shown in Figure 1. XCO₂ retrievals from each satellite also have different data precision for different sensors, observation conditions, and retrieval methods. Therefore, we use different XCO₂ precisions in time and space in the XCO₂ integration and mapping with the spatio-temporal kriging method.

Table 1. Specifications of multiple satellites that observed XCO₂.

Attributes\ Satellites	ENVISAT/SCIAMACHY	GOSAT	OCO-2
Period of selected data	January 2003–March 2012	June 2009–May 2016	September 2014–December 2016
Repeat cycle (days)	35	3	16
Field of view (km)	30 × 60	Diameter of 10.5	2.25×1.25
Overpass local time	10:00	13:00	13:36
version	BESD v02.01.01	ACOS v7.3	OCO2 r9
Profile layers number	10	20	20
Criteria of data screening	XCO ₂ _quality_flag=0;	XCO ₂ _quality_flag=0; gain=H; land_fraction>90; warn_level<10	XCO ₂ _quality_flag=0; gain=H; land_fraction>90
Name referred hereafter	SCI-XCO ₂	GOS-XCO ₂	OCO-XCO ₂
Reference	[37]	[38]	[39]

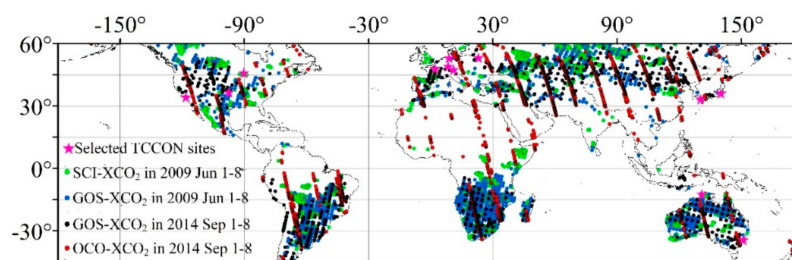


Figure 1. Example of XCO₂ from SCIAMACHY, GOSAT, and OCO-2. Green and blue points represent SCI-XCO₂ and GOS-XCO₂ from 1–8 June 2009. Black and red points are GOS-XCO₂ and OCO-XCO₂ from 1–8 September 2014. Total carbon column observing network (TCCON) sites used for validation are shown with a pink star.

2.2. The Total Carbon Column Observing Network

The total carbon column observing network (TCCON) are upward-looking terrestrial Fourier transform spectrometers established for measuring atmospheric XCO₂ and other trace gases from the surface [40]. The instruments have high accuracy with approximately 0.25% error in XCO₂ retrievals, which has been extensively used for validation of satellite observations [21,40,41]. In this study, we selected 12 TCCON sites within the mapping area as shown in Figure 1, with at least five years of coincidental measurements in the period from January 2003 to December 2016 for validating combined XCO₂ products.

2.3. XCO₂ from Model Simulation

CarbonTracker (CT) is a modeling system that assimilates global atmospheric CO₂ observations from the ground, tall tower, and aircraft, coupled with an atmospheric transport model for simulating global distributions of atmospheric CO₂ and tracking CO₂ sources and sinks. Model-simulated atmospheric CO₂ from CarbonTracker 2017 [42] was used in three steps of the integration and mapping method, primarily to normalize differences in altitude sensitivity and overpass time. First, we used CarbonTracker CO₂ profiles in a grid of 2° × 3° (latitude × longitude) in 3-hour intervals as the common profile to align the a priori CO₂ profiles and averaging kernels of multi-satellite observations. Second, we adopted diurnal patterns of CO₂ concentrations in different pressure layers from CarbonTracker to unify the CO₂ from satellite observations to 13:00 local time. XCO₂ from CarbonTracker (CT-XCO₂) was calculated from the model CO₂ profile data with 25 layers at the local time 13:00 by using a pressure weighting average method [43]. Third, we used the CT-XCO₂ for comparing with our new globally mapped XCO₂ product.

3. Method

In this study, we developed a method for spatio-temporal integration and mapping of multi-satellite observed XCO₂ considering variable data precision for producing globally mapped continuous XCO₂ with spatial/temporal resolution of 1° × 1° every eight days from 2003 to 2016. We present the flow chart of global mapped XCO₂ production and the precision weighted spatio-temporal kriging method in Figure 2. First, we adjusted a priori vertical CO₂ profiles and averaging kernels of multiple satellite-observed XCO₂ products to a common profile. Second, we corrected to a common local time and regularizing spatio-temporal scales of XCO₂ from multiple satellites. Third, we used a modeled continuous XCO₂ spatio-temporal random field for interpolation. Fourth, we developed a precision-weighted spatio-temporal kriging method for producing global maps of XCO₂. Finally, we validated the new global mapped XCO₂. We present details on developing the precision-weighted spatio-temporal kriging method including: (1) conventional spatio-temporal kriging method; (2) optimization of spatio-temporal correlation structure; (3) XCO₂ prediction through integrating data precision, and; (4) uncertainty and precision of mapped XCO₂.

3.1. Preprocessing

3.1.1. Adjustment of a Priori Vertical Profiles and Averaging Kernels

Each satellite has different measurement sensitivity at different altitudes through the atmospheric column and, therefore, they use different averaging kernels based on a priori assumptions of vertical CO₂ profiles to account for sensor sensitivities in XCO₂ retrieval algorithms. The corrections are based on prior vertical profile layers as shown in Table 1. The a priori profiles from different satellite retrievals should be adjusted to a common profile when comparing XCO₂ from different instruments. Additionally, the smoothing effect of the retrievals should be considered by applying the averaging kernels [44] to reduce the effects from different instruments on XCO₂ retrievals [37,45]. In this study,

we introduce a common a priori XCO_2 profile from CT to integrate XCO_2 retrievals from ENVISAT/SCIAMACHY, GOSAT, and OCO-2 by using Equation (1).

$$XCO_{2adj,t} = XCO_{2ret,t} + \mathbf{h}^T \cdot (\mathbf{I} - \mathbf{A}) \cdot (X_{M,t} - X_{a,t}) \quad (1)$$

where $XCO_{2adj,t}$ is the adjusted XCO_{2ret} at observation time t , $XCO_{2ret,t}$ is the original XCO_2 retrievals from satellites, \mathbf{h} is a pressure-weighting vector, \mathbf{A} is column-averaging kernels in the XCO_2 retrieval algorithm, \mathbf{I} is an identity matrix, $X_{M,t}$ is a set of common a priori CO_2 profiles from CT, and $X_{a,t}$ is a set of a priori CO_2 profiles used in XCO_2 original satellite-specific retrieval algorithms. A priori CO_2 profiles of each satellite, as shown in Table 1, were interpolated into the same 25 pressure layers of the CT model.

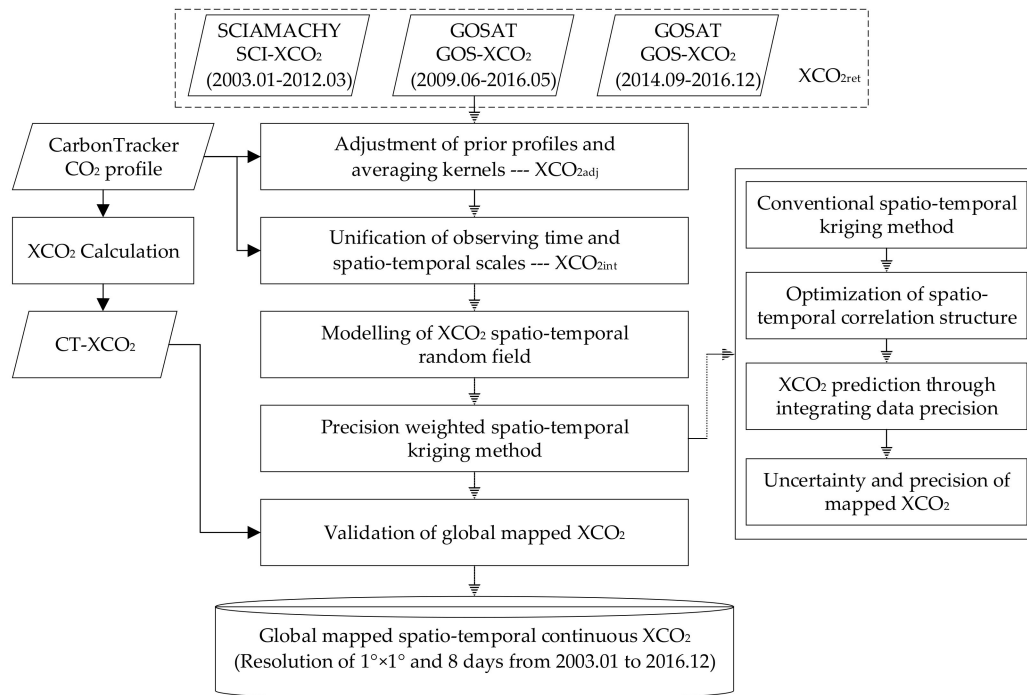


Figure 2. Workflow chart of spatio-temporal integration of multi-satellite observed XCO_2 using a precision-weighted kriging method.

3.1.2. Unification of Observing Time and Spatio-Temporal Scales

The three satellites have different local overpass times: SCIAMACHY at 10:00, GOSAT at 13:00, and OCO-2 at 13:36 (Table 1). In order to reduce the effect of atmospheric CO_2 concentrations diurnal variation [46,47], we introduce a correction coefficient to normalize the satellite observations local time to 13:00 based on diurnal variation of CT model simulations using Equation (2).

$$XCO_{2con,rt} = \frac{\mathbf{h}^T X_{M,rt}}{\mathbf{h}^T X_{M,t}} \cdot XCO_{2adj,t} \quad (2)$$

where $XCO_{2con,rt}$ is the converted XCO_{2adj} at the reference time (rt, 13:00 local time); $XCO_{2adj,t}$ is the adjusted XCO_2 derived from Equation (1) at satellite overpass time t ; $X_{M,rt}$ and $X_{M,t}$ are CO_2 profiles from CT at times of rt and t , respectively; and \mathbf{h} is the pressure-weighting vector.

Moreover, XCO_2 is affected by the different fields of view and observing dates as shown in Table 1. In order to reduce this effect, we integrate spatial and temporal scales of XCO_2 retrievals using precision weighted averaging of $XCO_{2con,rt}$ within 30 km by 30 km every 8 days using Equations (3-1) and (3-2). This unification also reduces computational complexity and preserves local spatiotemporal patterns. A temporal resolution of 8 days is also well-suited for biosphere-atmosphere interaction analysis

with other 8-day resolution datasets like vegetation indices from the Moderate Resolution Imaging Spectroradiometer (MODIS). An integrated XCO₂ dataset at 30 km resolution every 8 days from 2003 to 2016 (integrated-XCO₂) was generated.

$$XCO_{2_{int,rt}} = \sum_{i=1}^n p_i \cdot XCO_{2_{con,rt_i}} \quad (3-1)$$

$$\sum_{i=1}^n p_i = \sum_{i=1}^n \frac{\mu^2}{m_i^2} = 1 \quad (3-2)$$

where XCO_{2_{int,rt}} is the integrated combination of XCO_{2_{con}} datasets, n is the number of observations in one unit, XCO_{2_{con,rt_i}} is converted satellite observed XCO₂, p_i is the weighting factor, which is determined by m_i (data precision of XCO_{2_{con,rt_i}}). μ is an arbitrary constant used for normalizing the data precision weighting factor. We adopted the data precision from these satellites observed XCO₂ Level 2 product. The data precision in ACOS-GOSAT and OCO-2 is XCO₂ posterior error, and that in BESD-SCIAMACHY is 1-sigma uncertainty of the retrieved XCO₂.

3.2. Modeling XCO₂ Spatio-Temporal Random Field for use in Kriging

XCO₂ increases from year-to-year varies by latitude and has a significant seasonal cycle in most locations [48,49]. In order to interpret spatio-temporal geostatistics, we need to construct a second-order stationary random field represented by the stochastic residual component after removing inter-annual, latitudinal, and seasonal trends mentioned above, termed the deterministic mean. In this study, we adopted a fitting method for decomposing [50] the deterministic spatiotemporal mean and stochastic residual component of latitude-zonal XCO₂. The fitting method is a combination of a linear function to fit the long-term increase and annual periodic function as shown in Equation (4).

$$m(s, t) = a_0(s) + a_t(s) + \sum_{i=1}^4 (\beta_i(s) \cdot \sin(i\omega t) + \gamma_i(s) \cdot \cos(i\omega t)) + R(s, t) \quad (4)$$

where $\omega = 2\pi/T$ and T is the period of 46 time-units, t is the time in the time-unit, s represents the latitudinal zone, and a₀, β₁₋₄ and γ₁₋₄ are parameters to be estimated. a_t is the cumulative annual increase for each time-unit determined by the Earth System Research Laboratory (ESRL) global annual CO₂ growth rate [4]. The harmonic functions fit the annual cycle, semi-annual oscillation, seasonal variation and monthly variation of XCO₂ [19]. R(s, t) represents the spatio-temporal residual component of satellite observed integrated XCO₂, which will be used for interpretation.

3.3. Precision Weighted Spatio-Temporal Kriging

In the ordinary kriging method, a predicted value at an arbitrary target point is estimated by considering the statistical properties of a set of observed data. As a result, the predicted value (Z(s₀)) at point s₀ can be expressed as a weighted sum of the observational data as shown in Equation (5).

$$Z(s_0) = \sum_{i=1}^n \omega_i \cdot Z(s_i) \quad (5)$$

where ω_i is the weighting factor at the observation point s_i, n is the total number of observational points to be used, and Z(s_i) is the observed value at each point s_i. The following subsections describe the precision-weighted spatio-temporal kriging method. Different kriging models were developed by adjusting the number of points 'n' and the weighting factor 'ω_i'.

3.3.1. Conventional Spatio-Temporal Kriging

In spatio-temporal geostatistical analysis of XCO₂, kriging prediction of $Z(s_0, t_0)$ at a point (s_0, t_0) can be calculated as the linear weighted sum of the XCO₂ values that minimizes the mean squared prediction error [19]. Weights of observations used for interpolation are determined by the geometry of observations and the spatio-temporal correlation structure of the data. Spatial and temporal information would be used for variogram modeling of the correlation structure [19,31] as shown in Equation (6).

$$\hat{\gamma}_{ST}(h_s, h_t) = \frac{1}{2N(h_s, h_t)} \sum_{i=1}^{N(h_s, h_t)} [Z(s_i + h_s, t_i + h_t) - Z(s_i, t_i)]^2 \quad (6)$$

where $\hat{\gamma}_{ST}(h_s, h_t)$ is an empirical variogram value at the lag (h_s, h_t) . $Z(s_i, t_i)$ is the observational data. $N(h_s, h_t)$ is the number of data pairs within a distance of (h_s, h_t) . Once the empirical variogram has been constructed, we need to select a spatio-temporal variogram model to fit it. As shown in Zeng et al. [19,31], the spatio-temporal variogram model adopted here (Equation (7)) is a combination of the product-sum model [51,52] and an extra global nugget model to capture the nugget effect [53] (last term in Equation (7)).

$$\gamma_{ST}(h_s, h_t; \theta_s, \theta_t, \kappa, N_{ST}) = \gamma_S(h_s; \theta_s) + \gamma_T(h_t; \theta_t) - \kappa \cdot \gamma_S(h_s; \theta_s) \cdot \gamma_T(h_t; \theta_t) + N_{ST} \cdot \gamma_0(h_s; h_t) \quad (7)$$

We selected the exponential model for the marginal variogram model $\gamma_S(h_s)$ and $\gamma_T(h_t)$ as shown in Equation (8).

$$\gamma(h; \theta = [C, a]) = \begin{cases} 0, & h = 0 \\ C \cdot (1 - e^{-\frac{h}{a}}), & h \neq 0 \end{cases} \quad (8)$$

where $\gamma_S(h_s; \theta_s)$ and $\gamma_T(h_t; \theta_t)$ are the marginal spatial and temporal variograms, $[\theta_s, \theta_t, \kappa, N_{ST}] = [C_s, a_s, C_t, a_t, \kappa, N_{ST}]$ are parameters to be estimated, and N_{ST}, C , and a are all greater than or equal to zero. In the exponential model, a, C and N_{ST} represent the influence range, partial sill, and nugget effects, respectively.

As a result, an arbitrary target point $(\hat{Z}(s_0, t_0))$ to be estimated by using the spatio-temporal kriging method can be expressed as Equation (9).

$$\hat{Z}(s_0, t_0) = \sum_{i=1}^n \omega_i(s_0, t_0) \cdot Z(s_i, t_i) \text{ with } \sum_{i=1}^n \omega_i(s_0, t_0) = 1 \quad (9)$$

where $\omega_i(s_0, t_0)$ is the weight assigned to a known observation $Z(s_i, t_i)$ so as to minimize the prediction error variance while maintaining an unbiased prediction. The prediction error variance, which is a measurement of prediction uncertainty, is given by

$$\sigma^2 = \gamma_0^T \Gamma^{-1} \gamma_0 - \frac{(\mathbf{1}^T \Gamma^{-1} \gamma_0 - 1)^2}{\mathbf{1}^T \Gamma^{-1} \mathbf{1}} \quad (10)$$

where $\Gamma(i, j) = \gamma(|s_i - s_j|, |t_i - t_j|)$, $\gamma_0(i, 1) = \gamma(|s_i - s_0|, |t_i - t_0|)$, and $\mathbf{1}$ is the $n \times 1$ unit vector.

3.3.2. Optimization of Spatio-Temporal Correlation Structure

In a conventional spatio-temporal geostatistical analysis, all data pairs were used for spatio-temporal correlation structure using equal weight. XCO₂ observations from different satellites/sensors, observing conditions and inversion methods have different data precision. So, the

varying data precision should be considered in building the loss function for optimizing spatio-temporal correlation structure with precision weighting factor as shown in Equation (11).

$$\delta = \sum_{i=1}^m \lambda_i \cdot (\gamma_{ST} - \hat{\gamma}_{ST})^2 = \sum_{i=1}^m \lambda_i \cdot (\gamma_s(h_s) + \gamma_T(h_t) - \kappa \cdot \gamma_s(h_s) \cdot \gamma_T(h_t) + N_{ST} - \hat{\gamma}(h_s, h_t))^2 \quad (11-1)$$

$$\sum_{i=1}^n \lambda_i = \sum_{i=1}^n \frac{\mu_1^2}{m_i^2} = 1 \quad (11-2)$$

where λ_i represents different weighting factors for data with different precisions. γ_{ST} is the spatio-temporal variogram model shown in Equation (7). $\hat{\gamma}_{ST}$ is the empirical variogram shown in Equation (6). m_i and μ_1 represent data precision and a normalization term.

The gradient descent method was used to calculate the optimal parameters. The partial derivative parameters ($\delta'_{C_s^*}, \delta'_{a_s^*}, \delta'_{C_t^*}, \delta'_{a_t^*}, \delta'_{\kappa^*}, \delta'_{N_{ST}^*}$) that need to be estimated are shown in Equations (12-1)–(12-6).

$$\delta'_{C_s^*} = 2 \cdot \sum_{i=1}^m \{\lambda_i \cdot (\gamma_{ST}(h_s, h_t) - \hat{\gamma}(h_s, h_t))\} \cdot \left(1 - e^{-\frac{\|h_s\|}{a_s^*}}\right) \quad (12-1)$$

$$\delta'_{a_s^*} = 2 \cdot \sum_{i=1}^m \{\lambda_i \cdot (\gamma_{ST}(h_s, h_t) - \hat{\gamma}(h_s, h_t))\} \cdot \left(-C_s^* \cdot e^{-\frac{\|h_s\|}{a_s^*}}\right) \cdot (\|h_s\| \cdot a_s^{*-2}) \quad (12-2)$$

$$\delta'_{C_t^*} = 2 \cdot \sum_{i=1}^m \{\lambda_i \cdot (\gamma_{ST}(h_s, h_t) - \hat{\gamma}(h_s, h_t))\} \cdot \left(1 - e^{-\frac{\|h_t\|}{a_t^*}}\right) \quad (12-3)$$

$$\delta'_{a_t^*} = 2 \cdot \sum_{i=1}^m \{\lambda_i \cdot (\gamma_{ST}(h_s, h_t) - \hat{\gamma}(h_s, h_t))\} \cdot \left(-C_t^* \cdot e^{-\frac{\|h_t\|}{a_t^*}}\right) \cdot (\|h_t\| \cdot a_t^{*-2}) \quad (12-4)$$

$$\delta'_{\kappa^*} = 2 \cdot \sum_{i=1}^m \{\lambda_i \cdot (\gamma_{ST}(h_s, h_t) - \hat{\gamma}(h_s, h_t))\} \cdot (\gamma_s(h_s; \theta_s^*) \cdot \gamma_T(h_t; \theta_t^*)) \quad (12-5)$$

$$\delta'_{N_{ST}^*} = 2 \cdot \sum_{i=1}^m \{\lambda_i \cdot (\gamma_{ST}(h_s, h_t) - \hat{\gamma}(h_s, h_t))\} \quad (12-6)$$

where $C_s^*, a_s^*, C_t^*, a_t^*, \kappa^*$ and N_{ST}^* are parameters waiting to be optimized. Parameters, $\lambda_i, \gamma_{ST}, \gamma$ and $\hat{\gamma}$, are the weighting factors (Equation (11-2)), exponential models (Equation (7) and Equation (8)) and empirical variogram values (Equation (6)), respectively.

We optimized the structure through minimizing δ . Initial parameters $\beta_0 = (C_{s0}, a_{s0}, C_{t0}, a_{t0}, \kappa_0, N_{ST0})$ were obtained by using a least-squares approximation in the conventional spatio-temporal kriging method. Then, parameters were determined by a learning rate and partial derivative as shown in Equation (13).

$$\beta_i = \beta_{i-1} + \alpha \cdot \delta'_{i-1} \quad (13)$$

where β represents $(C_s^*, a_s^*, C_t^*, a_t^*, \kappa^*, N_{ST}^*)$. α is the learning rate, usually in the range of $(10^{-4} \sim 10^{-2})$. δ' is the partial derivative parameter. We set the operating condition as a current change of less than 1% of all the changes in this adjustment. As a result, one example of optimized spatio-temporal semi-variogram surface is shown in Figure 3.

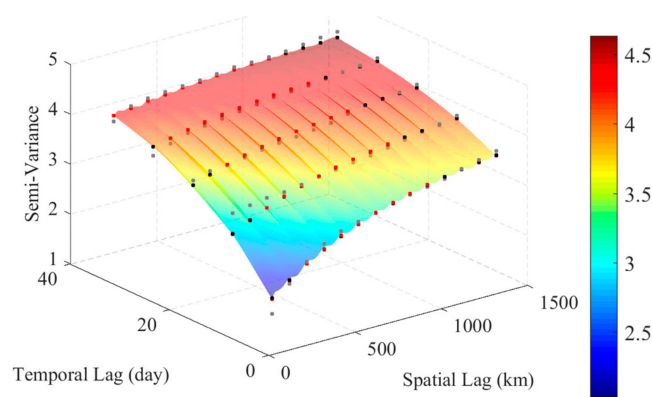


Figure 3. One example of the optimized spatio-temporal semi-variogram surface (Zone 1: Latitude center: 55°N). Grey, black, and red points represent spatio-temporal semi-variogram that was calculated from experimental data, fitted models of the conventional and optimized correlation structure.

3.3.3. Integrating XCO₂ Using Variable Data Precision

We estimated XCO₂ in unobserved points using observational data and weighting factors from spatio-temporal correlation structure and data precision as shown in Equation (14).

$$Z(s_0, t_0) = \sum_{i=1}^n \omega_{1i} \cdot \omega_{2i} \cdot Z(s_i, t_i) \tag{14}$$

where ω_{1i} is the weighting factor from the spatio-temporal correlation structure and ω_{2i} is from data precision. $Z(s_i, t_i)$ is observed XCO₂ used for $Z(s_0, t_0)$ estimation. These two weighting factors were calculated by Equations (15-1) and (15-2).

$$\begin{aligned} \sum_{i=1}^s \omega_{1i} \cdot \gamma(h_{1i}) + \varepsilon &= \gamma(h_{10}) \\ \sum_{i=1}^s \omega_{1i} \cdot \gamma(h_{2i}) + \varepsilon &= \gamma(h_{20}) \\ &\dots\dots \\ \sum_{i=1}^s \omega_{1i} \cdot \gamma(h_{si}) + \varepsilon &= \gamma(h_{s0}) \end{aligned} \tag{15-1}$$

$$\sum_{i=1}^s \omega_{1i} \cdot \omega_{2i} = 1 \tag{15-2}$$

where ω_{1i} and ω_{2i} are weighting factors in Equation (14). Equation (15-2) was used to control unbiased estimation. $\gamma(h_{1i}) \dots \gamma(h_{si})$ and $\gamma(h_{10}) \dots \gamma(h_{s0})$ are spatio-temporal variograms for observations used for estimation of $Z(s_0, t_0)$. ε is the polynomial residuals. ω_{2i} can be achieved by Equation (16).

$$\sum_{i=1}^s \omega_{2i} = \sum_{i=1}^s \frac{\mu_2^2}{m_i^2} = s \tag{16}$$

where m_i , μ_2 and s are data precision, arbitrary constant and the number of used observational data.

We applied this method for global mapping of XCO₂ (GM-XCO₂), which provides a long time series of spatio-temporal continuous XCO₂ dataset for global carbon cycle research.

3.3.4. Uncertainty and Precision of Mapped XCO₂

We calculated data uncertainty and precision of the mapped XCO₂ by using precision-weighted kriging. Uncertainty of predicted data from the spatio-temporal kriging method is shown in Equation (17)

$$\sigma_0^2 = \sum_{i=1}^s w_{1i} \cdot \gamma(h_{i0}) + \varepsilon \quad (17)$$

where σ_0^2 presents the prediction uncertainty, w_{1i} , $\gamma(h_{i0})$ and ε are the estimated weighting factor, spatio-temporal variograms, and polynomial residuals, respectively as shown in Equation (15).

In addition, the precision of GM-XCO₂ integrated from the observed data is shown in Equation (18), according to the error transfer equation.

$$\varepsilon_0 = \text{sqrt}\left(\sum_{i=1}^s \varepsilon_i^2 \cdot w_{1i}^2 \cdot w_{2i}^2\right) \quad (18)$$

As a result, these two sources of uncertainty can be used for data screening in GM-XCO₂ application.

3.4. Validation of Global Mapped XCO₂

We validated the mapped GM-XCO₂ product using cross-validation, compared to TCCON measurements and model simulation. Cross-validation has been used in accuracy assessments for spatio-temporal kriging methods [19,54]. In this study, we adopted cross-validation based on the Monte Carlo sampling method used in Zeng et al. [19]. As above, we used the satellite-observed integrated XCO₂ dataset (XCO_{2_{int}}) for interpolation to GM-XCO₂. The cross-validation was conducted by repeatedly (100 times) reserving 5% of the XCO_{2_{int}} data for validation. Predicted GM-XCO₂ was compared with the 5% reserved XCO_{2_{int}} data in those corresponding spatio-temporal locations. We selected three statistical parameters for results evaluation: (1) the coefficient of determination (r^2), (2) the root mean square error (RMSE), and (3) the percentage of estimation bias less than 1 or 2 times of data precision.

We compared GM-XCO₂ with the XCO₂ measured from TCCON (TCCON-XCO₂) in 12 sites with more than 5 years of observation. TCCON-XCO₂ was calculated with the pressure-averaged method [43] and data observed at a local time of 11:00 to 15:00. In addition, we did a comparison between GM-XCO₂ and XCO₂ from the CT model simulation in the spatio-temporal change over the global area.

4. Results

4.1. Integrated-XCO₂ from Three Satellites

Here we presented latitudinal and temporal variability of the integrated XCO₂ (top panel) and the difference between the integrated product and the original retrieval XCO₂ values (bottom panel) from SCIAMACHY, GOSAT, and OCO-2 (Figure 4). The top panel shows XCO₂ increased more than 30 ppm from 2003 to 2016 over most latitudes. Especially high XCO₂ values occurred during the start of 2016 in the northern hemisphere (dark red). The bottom panel shows XCO₂ adjustments, integrated XCO₂ (XCO_{2_{int}}) minus original XCO₂ (XCO_{2_{ret}}) were mainly within −2.0 to 1.0 ppm and include seasonality, with high adjustment values in summer and low adjustment values in winter, except for some scattered grids in high or low latitudes. This could be caused by seasonal changes of the XCO₂ averaging kernel (Appendix A: Figure A1) that was adopted for XCO₂ adjustment in Equation (1). In addition, the adjustments decreased sharply in 2012 and 2016, with stability improvements of the newer satellite sensors.

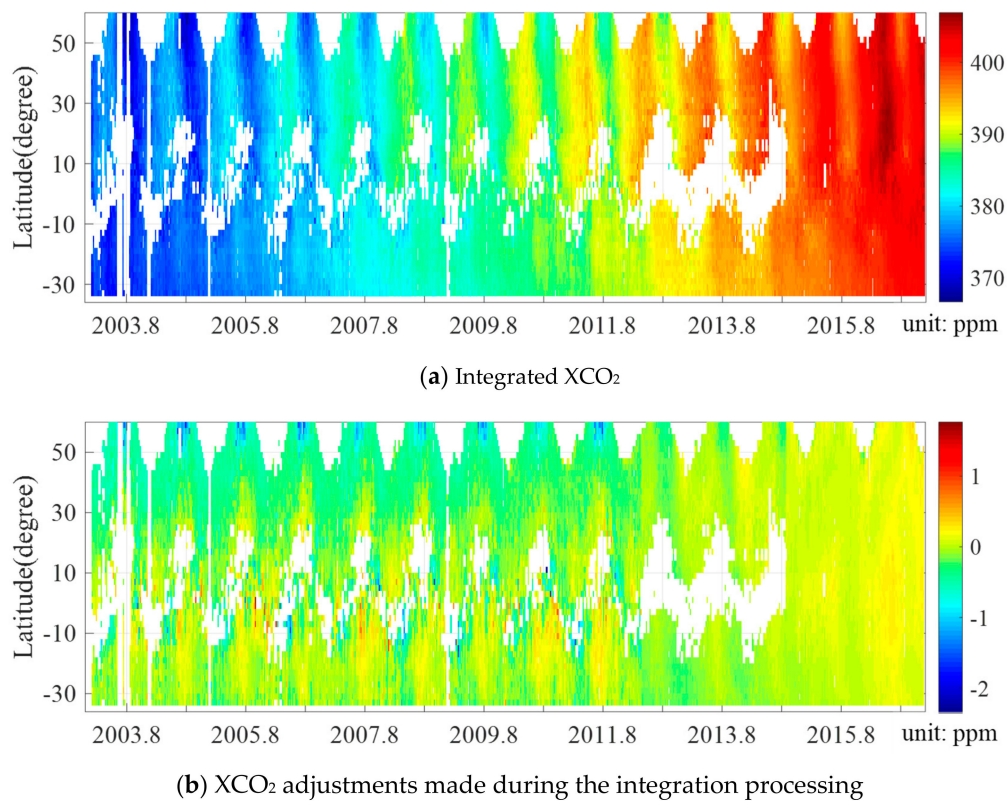


Figure 4. Latitudinal-temporal change of integrated XCO₂ (a) and XCO₂ adjustments made during the integration processing, integrated XCO₂ (XCO_{2_{int}}) minus original XCO₂ (XCO_{2_{ret}}) (b) from SCIAMACHY, GOSAT, and OCO-2.

4.2. Globally-Mapped XCO₂

4.2.1. Latitudinal and Temporal Variability of Globally Mapped XCO₂

The latitudinal and temporal variability of globally mapped XCO₂ (GM-XCO₂) and its prediction uncertainty and precision are shown in Figure 5. Comparing Figure 5a to gaps in Figure 4a show missing observations have been reasonably filled. GM-XCO₂ also shows the yearly increase and seasonal variation from 2003 to 2016. GM-XCO₂ is higher in the northern hemisphere compared to the southern hemisphere, and the annual maximum GM-XCO₂ lasts longer in mid-latitudes than high/low latitudes.

In the middle panel, kriging standard deviations (square root of σ_0^2 in Equation 17) of the predicted GM-XCO₂ represents the prediction uncertainty, which is determined by the available data around gaps. Higher uncertainty is shown in the tropic and high latitudes because of low numbers of robust observations in these latitudes corresponding to gaps in Figure 4a. The uncertainty also shows seasonal variation for different latitudes. In mid-high latitudes (35–60 °N), the uncertainty is high in winter for the observations affected by snow cover. In mid-low latitudes (extratropics within 35°N/S), uncertainty is high in summer likely due to cloud contamination during the monsoon season.

In the bottom panel, GM-XCO₂ precision is calculated from integrated XCO₂ (XCO_{2_{int}}) precision. The precision is significantly improved from the middle of 2009 and 2014. It was 1.5 to 2.5 ppm before 2009, 0.5 to 1.5 from 2009 to 2014, and below 0.5 after 2014. That is because of the observing precision improvement of the newer sensors. Generally, the observed GM-XCO₂ precision is better in mid-latitudes.

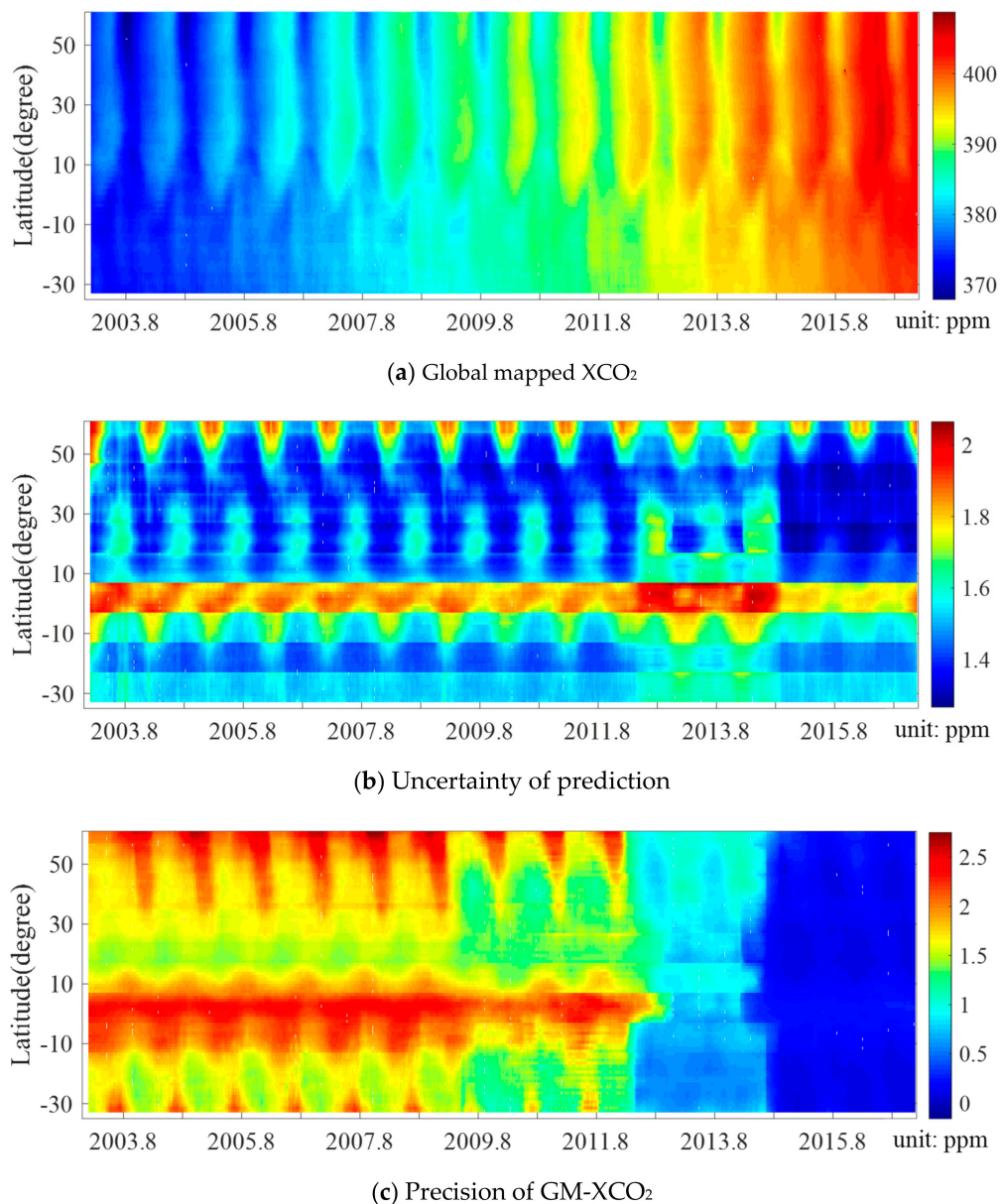


Figure 5. Latitudinal and temporal variability of global mapped XCO₂ (GM-XCO₂, top panel), the uncertainty of the prediction (standard deviation, middle panel), and precision (bottom panel).

4.2.2. Comparison with Conventional Spatio-Temporal Kriging Results

The latitudinal and temporal differences between the results from the precision-weighted (this study) and conventional spatio-temporal kriging methods are shown in Figure 6. Precision (Figure 6c) of GM-XCO₂ from precision weighted spatio-temporal kriging is improved for most of the predictions, especially for the SCIAMACHY and GOSAT overlapping periods (June 2009–March 2012) or GOSAT and OCO-2 overlaps (September 2014–May 2016). The precision improved by 0.3–0.5 ppm over latitudes with overlapping observations. GM-XCO₂ (Figure 6a) is enhanced by 0.1–0.2 ppm for the summer of 2009 to 2011 and reduced by 0.2–0.3 for the summer of 2014 to 2016. Differences in the uncertainty of prediction (Figure 6b) are small for both kriging results (conventional and precision-weighted) because they are based on the same observations (XCO_{2, int}), which results in a similar spatio-temporal correlation structure as shown in Figure 3.

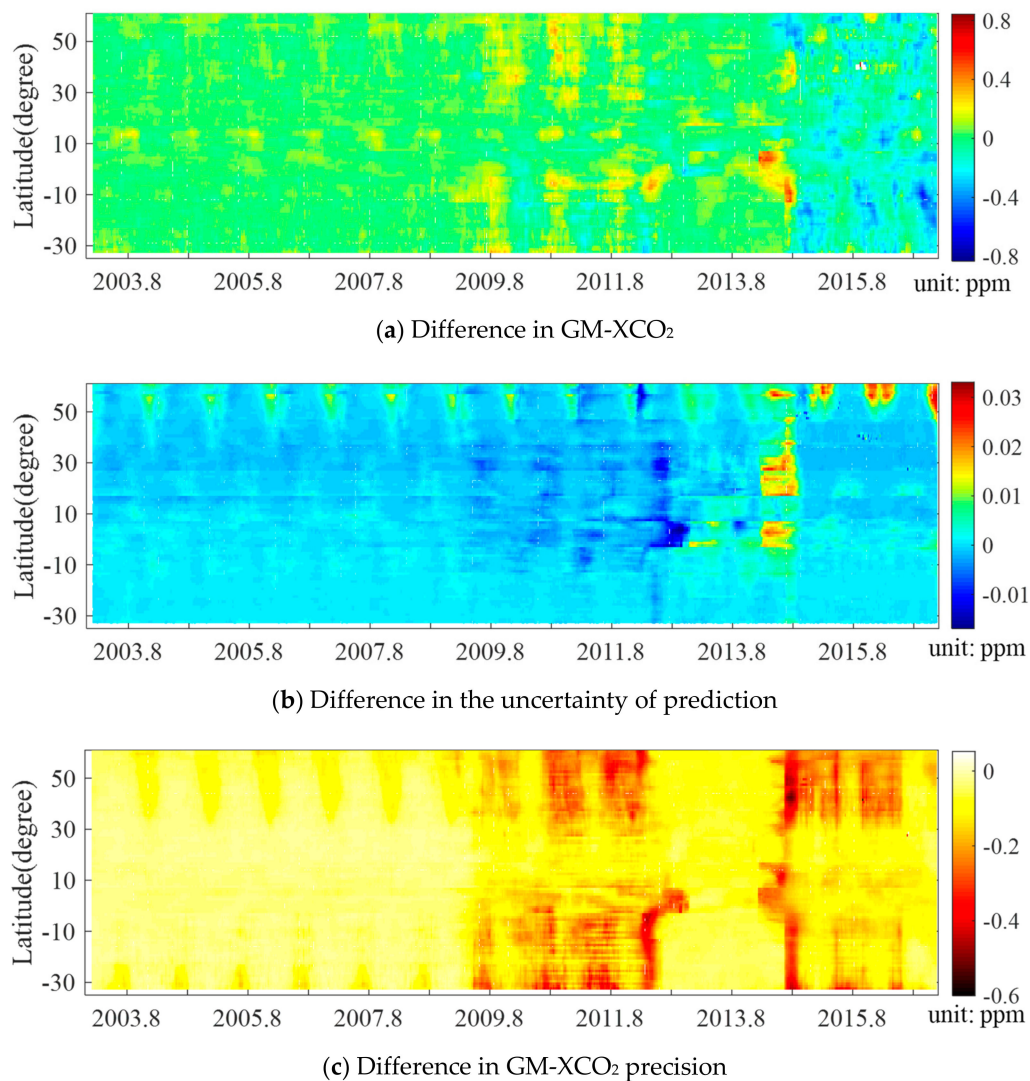


Figure 6. Latitudinal and temporal difference between results from precision-weighted and conventional spatio-temporal kriging methods for global mapped XCO₂ (GM-XCO₂, top panel), the difference in the uncertainty of the prediction (standard deviation, middle panel) and the difference in GM-XCO₂ precision (bottom panel). Positive values indicate precision-weighted results are higher and vice versa.

4.2.3. Spatial Distribution of GM-XCO₂

GM-XCO₂ provides important information about the mean spatial distribution and localized anomalies which could relate to local carbon uptake and emission. We present the spatial-temporal distribution of GM-XCO₂ during different seasons in 2003, 2008, 2013, and 2015 (Figure 7). Seasonal patterns of GM-XCO₂ were similar with an annual increase of approximately around 2.0 ppm. In spring, high GM-XCO₂ appeared in northern Canada, the North China Plain, and the Arabian Peninsula. In summer, extremely low GM-XCO₂ occurred in mid-high latitudes in the northern hemisphere. In autumn, the north-south hemispheric GM-XCO₂ gradient relaxes. In winter, high XCO₂ returns over the North China Plain and Central Africa.

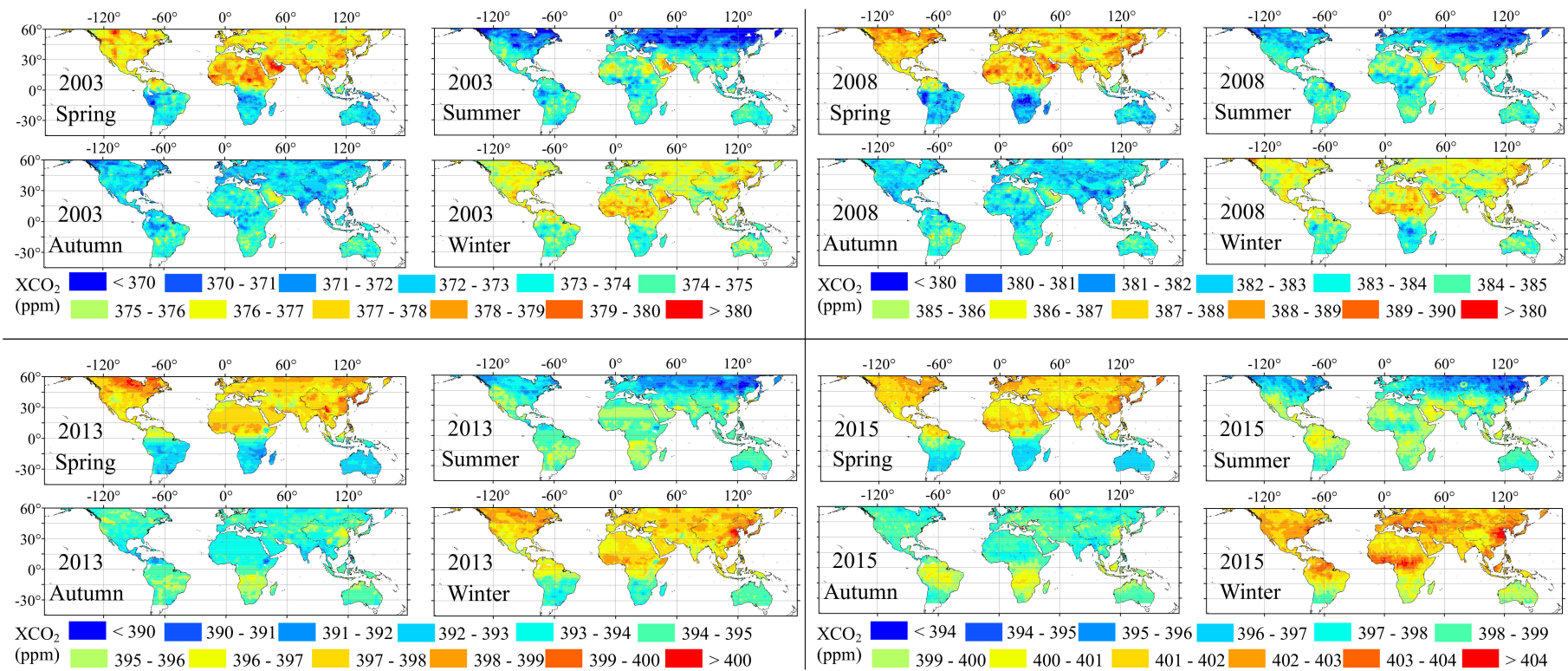


Figure 7. Spatial-temporal distribution of mean seasonal globally-mapped XCO₂ (GM-CO₂) during spring (March, April, May), summer (June, July, August), autumn (September, October, November) and winter (December, January, February) of 2003 (top-left), 2008 (top-right), 2013 (bottom-left), and 2015 (bottom-right). Color bars for different years assume an annual increase of 2 ppm.

In addition, we give out the global spatial distribution of mean XCO₂ in 2016 shown in Figure 8. We can find that the main high XCO₂ of 2016 is distributed in Eastern China, Southeast Asian regions, Amazon forest regions, African forest regions, south of the United States, the Arabian Peninsula, and India. These regions could be related to three main conditions, including (1) an industrial development zone inhabited by human beings; (2) a large area of tropical/subtropical rainforest area; (3) large agricultural regions.

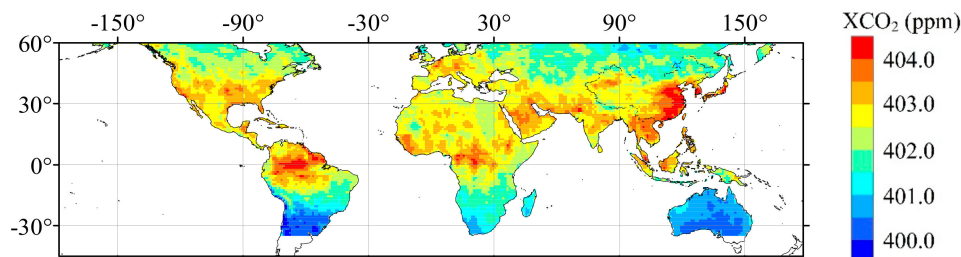
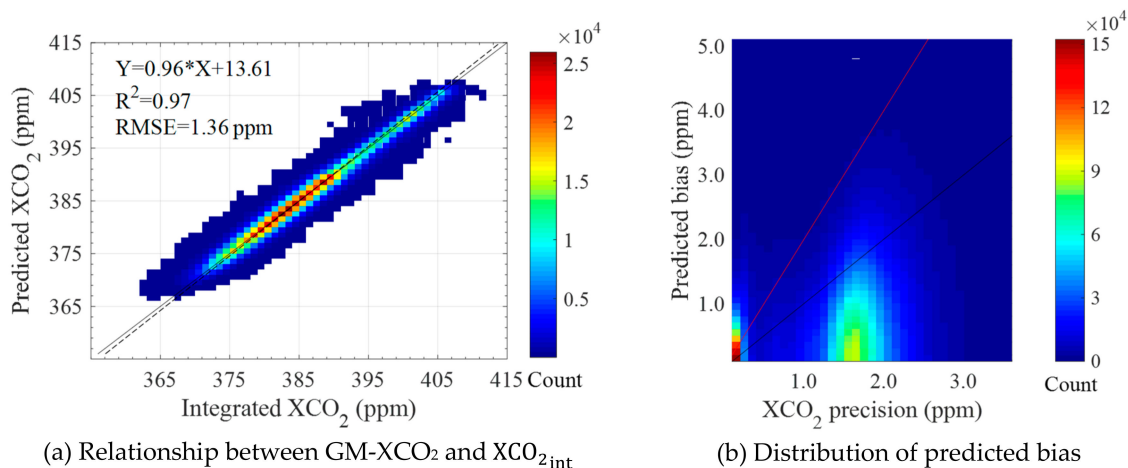


Figure 8. Spatial-temporal distribution of mean GM-XCO₂ in 2016.

4.3. GM-XCO₂ Validation

4.3.1. Evaluation Using Cross-Validation

Results of cross-validation using the precision-weighted spatio-temporal kriging method are shown in Figure 9. Predicted XCO₂ (GM-XCO₂) agreed well with integrated XCO₂ (XCO_{2_{int}}) with a high R² of 0.97, showing the interpolation method retains much of the input signal. Total RMSE (root mean square error) between predicted GM-XCO₂ and integrated XCO₂ (XCO_{2_{int}}) is 1.36 ppm, which indicates good stability and the high precision of this method. Most of the predicted bias is within 1.0 ppm, except for some XCO₂ data precision which is larger than 1.5 ppm (right panel). Specifically, 61% of the prediction bias is less than 1.0 ppm. Additionally, 70% and 80% of the predicted bias is within 1 and 2 times of XCO₂ precision, respectively. Results from cross-validation suggest that this mapping method is effective and precise in gap-filling of multi-satellites observed XCO₂, which could also be affected by original data precision.



(a) Relationship between GM-XCO₂ and XCO_{2_{int}}

(b) Distribution of predicted bias

Figure 9. Results of cross-validation using the precision-weighted spatio-temporal kriging method. The relationship between predicted XCO₂ (GM-XCO₂) and reserved integrated XCO₂ (XCO_{2_{int}}) is shown in the left panel. The distribution of predicted bias (absolute difference between GM-XCO₂ and reserved XCO_{2_{int}}) and XCO_{2_{int}} precision is shown in the right panel. The black and red lines in the right panel represent the slope of 1 and 2.

4.3.2. Validation of GM-XCO₂ with TCCON Measurements

High accuracy and continuous time series of XCO₂ from TCCON measurements were used for validation of GM-XCO₂ derived from satellite observations. In this study, we selected 12 sites with measurements for more than five years from 2003 to 2016 for comparison with GM-XCO₂. XCO_{2,int} and GM-XCO₂ data within 500 km of each TCCON site was used for this comparison (Figure 10). GM-XCO₂ retained information from satellite observations, which captured the annual increase and seasonal variation of XCO₂ well. The temporal variation of GM-XCO₂ is consistent with TCCON XCO₂. Comparison statistics between GM-XCO₂ and TCCON XCO₂ are shown in Table 2. If we assume TCCON measurements are accurate, the accuracy of GM-XCO₂ performs well with the total averaged bias of 0.01 ppm across 303 data pairs. The precision of GM-XCO₂ in most TCCON sites (9/12) is within 1.0 ppm with an averaged absolute bias of 0.92 ppm. The mean value of the standard deviation of the bias over 12 sites is 1.05 ppm.

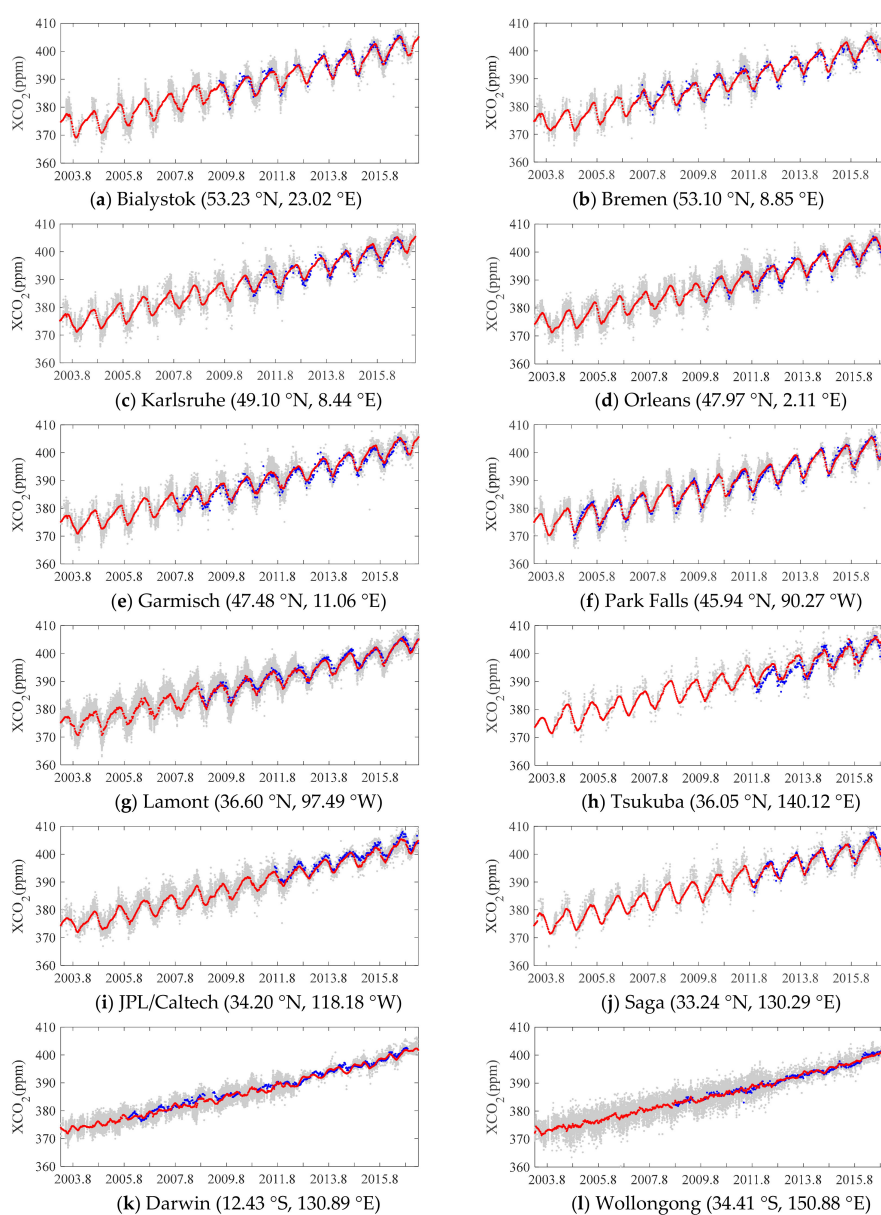


Figure 10. Temporal variation comparison of GM-XCO₂ at 12 TCCON sites. Grey, red, and blue points represent XCO_{2,int}, GM-XCO₂, and XCO₂ from TCCON measurements, respectively. XCO_{2,int} was retrieved within 500 km of TCCON sites. TCCON measurements from 11:00 to 15:00 local time were selected for comparison.

Table 2. Comparison statistics between GM-XCO₂ and TCCON XCO₂. Bias is calculated using GM-XCO₂ minus TCCON XCO₂ for each coincident data pair and averaged for each site.

Sites	Location (Latitude, Longitude)	Coincident Data Pairs	Averaged Bias (ppm)	Averaged Absolute Bias (ppm)	Standard Deviation (ppm)
Bialystok	(53.23°N, 23.02°E)	249	−0.19	0.73	0.92
Bremen	(53.10°N, 8.85°E)	260	0.21	0.97	1.25
Karlsruhe	(49.10°N, 8.44°E)	226	0.51	0.90	0.98
Orleans	(47.97°N, 2.11°E)	232	0.34	0.71	0.85
Garmisch	(47.48°N, 11.06°E)	361	0.62	1.05	1.16
Park Falls	(45.94°N, 90.27°W)	499	0.00	0.74	0.96
Lamont	(36.60°N, 97.49°W)	381	−0.45	0.77	0.92
Tsukuba	(36.05°N, 140.12°E)	210	0.73	1.70	1.89
JPL/Caltech	(34.20°N, 118.18°W)	243	−1.06	1.19	0.97
Saga	(33.24°N, 130.29°E)	204	−0.33	0.76	0.91
Darwin	(12.43°S, 130.89°E)	434	−0.47	0.89	1.00
Wollongong	(34.41°S, 150.88°E)	341	0.09	0.58	0.75
Overall	-	303	0.01	0.92	1.05

4.4. Comparison between GM-XCO₂ and CarbonTracker Simulated XCO₂

GM-XCO₂, the spatial-temporal continuous XCO₂ from satellite observations, can provide a detailed distribution of XCO₂ over global or regional land areas. In order to explore the advantages and disadvantages of GM-XCO₂, we present the latitudinal-temporal change comparison between GM-XCO₂ with CT-XCO₂ and their local temporal change comparison in the northern hemisphere.

4.4.1. Comparison with Latitudinal and Temporal Variability of CT-XCO₂

The latitudinal and temporal variability of the difference between GM-XCO₂ (Figure 5) and CT-XCO₂ (Appendix A: Figure A2) and statistical summary are shown in Figure 11. The mean difference is 1.53 ± 0.80 ppm. XCO₂ difference in the mid-latitudes showed better consistency with the mean value than that in low/high latitudes. The difference in high latitudes is smaller, especially for data before March 2012. In low latitudes, the difference varied with time, with lower values in summer and higher values in winter. The differences decreased with the satellite observations precision improvement from 2009 to 2016.

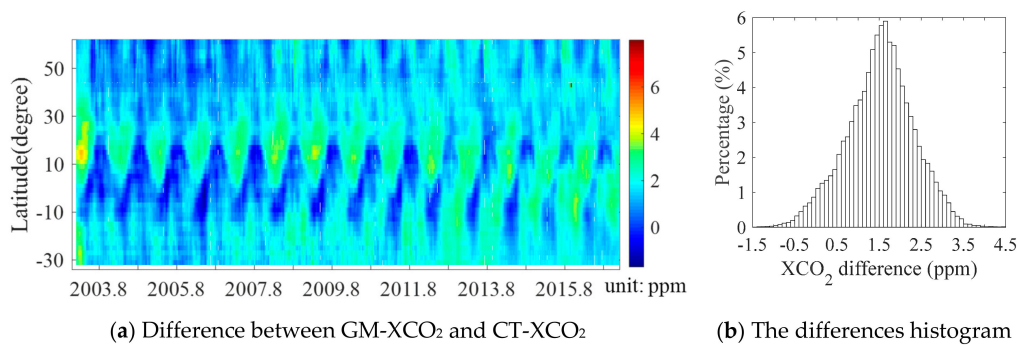


Figure 11. Latitudinal and temporal variability of the difference between GM-XCO₂ and CT-XCO₂ (a): GM-XCO₂ minus CT-XCO₂) and a histogram of the differences (b).

XCO₂ from low/high latitudes, especially for data before March 2012, shows the largest differences between GM-XCO₂ and CT-XCO₂. The potential reasons for this are: (1) Sparse satellite observation in high/low latitudes limited the accuracy of GM-XCO₂; (2) Limited precision of XCO₂ from SCIAMCHY contributed to large differences compared to CT-XCO₂; (3) Lacking or limited surface measurements in low/high latitudes constrained the CT model and affected the simulation of accurate XCO₂. GM-XCO₂ provided spatial-temporal continuous XCO₂ based on satellite observations that are different from the model simulation.

4.4.2. Temporal Variability of GM-XCO₂ and CT-XCO₂ in Mid-Latitudes

GM-XCO₂ may provide insights into local carbon uptake and emission. We present the temporal variability of XCO_{2int}, GM-XCO₂, and XCO₂ from CarbonTracker (CT-XCO₂) from 2003 to 2016 over mid-latitudes of North America and Eastern Asia (Figure 12). Mean GM-XCO₂ kept the original XCO_{2int} information from the satellites observation by kriging the XCO_{2int}. However, GM-XCO₂ presented sharp changes in XCO₂ during the peak and minimum of XCO₂ in each year, which is not as smooth as that of CT-XCO₂. In addition, the temporal variability of GM-XCO₂ was more consistent with CT-XCO₂ in Northern America than that of Eastern Asia. That could be attributed to the contribution from more surface measurements to constrain the models. As a result, GM-XCO₂ might provide more information for areas with limited surface measurements, such as China.

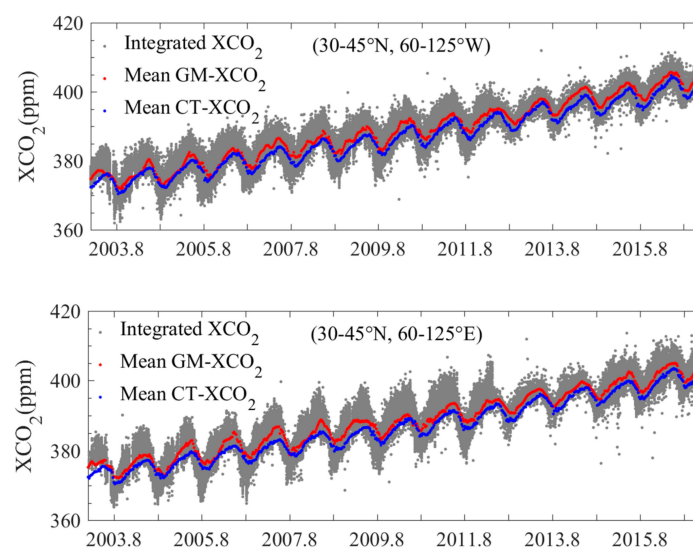


Figure 12. Temporal variation of XCO₂ from integrated and global mapped results (grey and red points) and CarbonTracker (blue points) over latitude in the range of 30 to 45°N and longitude of 60 to 125°W and 60 to 125°E.

5. Discussion

There are some advantages of GM-XCO₂ used in global carbon cycle studies. GM-XCO₂ provided spatial-temporal continuous XCO₂ data from 2003 to 2016 which filled the gaps in observation as shown in Figure 1. It improved the data precision compared with XCO₂ from conventional spatio-temporal kriging, especially for data in the satellites overlapping period. As a result, GM-XCO₂ could help us understand the temporal and spatial changes in the global distribution of CO₂ [17]. Because GM-XCO₂ is from instantaneous satellite observations, it could capture detailed and abnormal XCO₂ change which could be related to local carbon uptake and emission [10,55]. It could also be an important dataset for biosphere-atmosphere interactions by relating its changes to local biosphere parameter variations [7,11]. In addition, we provide XCO₂ precision and interpolation uncertainty for each XCO₂. Users can select different temporal and spatial segments of GM-XCO₂ data for their specific application. As it was discussed that space-based XCO₂ with precision (no bias) of 2.5 ppm could be used for matching ground-based network and precision within 1.0 ppm, it could help reduce inferred CO₂ flux uncertainties significantly [56]. For anthropogenic CO₂ monitoring, a precision requirement of GM-XCO₂ must be better than 0.7 ppm [57].

However, there are also some challenges that need to be discussed. Prediction of GM-XCO₂ in regions with little observations could have low precision and high interpolation uncertainty. GM-XCO₂ in the tropical rainforest area and the winter in high latitudes should be used carefully as a few observations were limited by observing conditions [58,59]. The interpolation method might not describe the process of atmospheric transport perfectly, especially for regions with a complex climate like the Tibetan area. In addition, GM-XCO₂ over a desert like the Sahara with an influence from high brightness reflection and complex dust for satellite observations inversion should also be used carefully [60].

6. Conclusions

In this study, we developed a precision-weighted spatio-temporal kriging interpolation method of multiple satellite observed XCO₂. It not only used the spatio-temporal variability of XCO₂, but also the precision of each observation for gap filling. The spatio-temporal correlation structure was optimized and the weighting of XCO₂ with high precision was improved. The precision of predictions improved in most of the grids, especially for the satellites overlapping period (0.3 – 0.5 ppm). It would be useful for gap-filling of increasing satellite observations not only in XCO₂ but also for other data observed by multiply satellites with different precision.

We also produced a spatial-temporal continuous XCO₂ product, which provides the data precision and interpolation uncertainty of each grid. It is spatio-temporal continuous XCO₂ from satellite observations which could capture the detailed change of XCO₂. It could be an available dataset for global carbon cycle studies like biosphere-atmosphere interaction.

Author Contributions: L.L., and Z.H. conceived and designed the experiments; Z.H. performed the experiments; L.R.W., Z.H., and L.L. analyzed the data; C.W., M.S., Y.Z., L.L. and Z.-C.Z. contributed analysis tools; Z.H., and L.R.W. wrote the paper. All authors have read and agreed to the published version of the manuscript.

Funding: This research was funded by the Strategic Priority Research Program of the Chinese Academy of Sciences (XDA19080303), the Key Research Program of Chinese Academy of Sciences (ZDRW-ZS-2019-3) and the National Key Research and Development Program of China (2016YFA0600303).

Acknowledgments: We also thank ESA for sharing the SCIAMACHY BESD XCO₂ level 2 data, the ACOS/OCO-2 project at JPL for sharing ACOS-GOSAT v7.3 and OCO-2 v9r data, NOAA ESRL for providing CarbonTracker CT2017 results. TCCON data were obtained from the TCCON Data Archive website at <http://tcccon.ornl.gov/>.

Conflicts of Interest: No conflict.

Appendix A

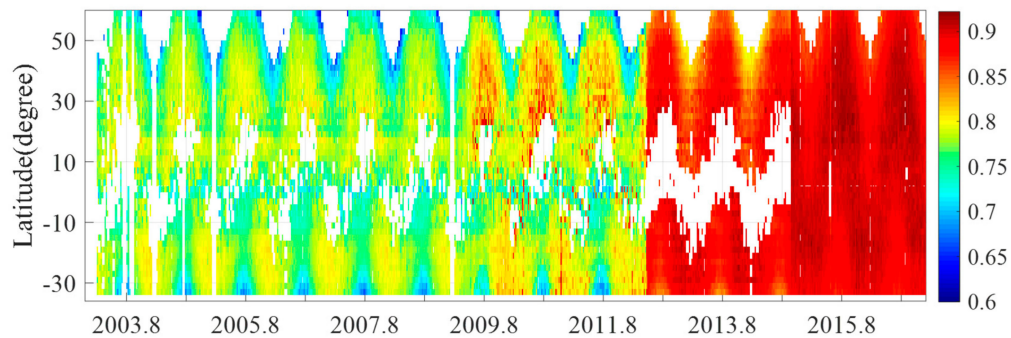


Figure A1. Latitudinal-temporal change of mean XCO₂ averaging kernel from SCIAMACHY (January–March 2003), GOSAT (June 2009–May 2014), and OCO-2 (September 2014.09–December 2016).

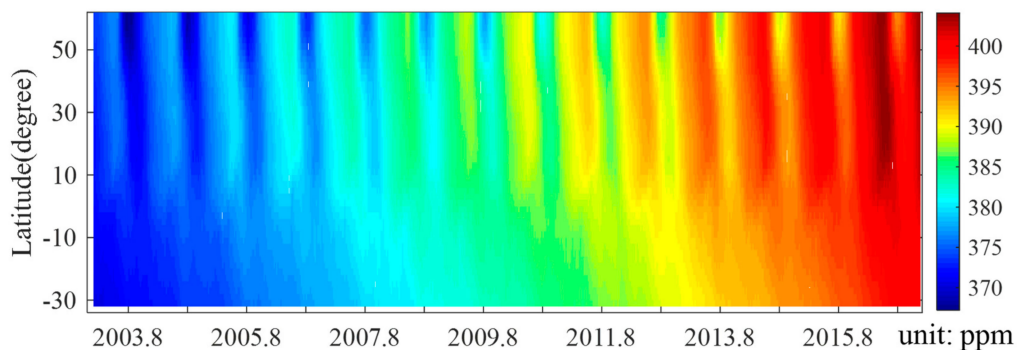


Figure A2. Latitudinal-temporal change of CT-XCO₂ from 2003 to 2016

Acronyms

Acronyms	Full Names
XCO ₂	Column-averaged dry air mole fraction of atmospheric CO ₂
XCO _{2_{ret}}	Original XCO ₂ retrievals from satellites
XCO _{2_{adj}}	Adjusted XCO _{2_{ret}}
XCO _{2_{con}}	Converted XCO _{2_{adj}}
XCO _{2_{int}}	Integrated combination of XCO _{2_{con}}
GM-XCO ₂	Global mapped XCO ₂
ENVISAT	Environmental Satellite
SCIAMACHY	SCanning Imaging Absorption spectroMeter for Atmospheric CHartography
GOSAT	Greenhouse Gases Observing Satellite
OCO-2	Orbiting Carbon Observatory-2
BESD	Bremen Optimal Estimation–DOAS
ACOS	Atmospheric CO ₂ Observations from Space
TCCON	The total carbon column observing network
CT	CarbonTracker
r ²	the coefficient of determination
RMSE	the root mean square error
ESRL	Earth System Research Laboratory

References

1. Le Quéré, C.; Andrew, R.M.; Friedlingstein, P.; Sitch, S.; Hauck, J.; Pongratz, J.; Pickers, P.A.; Korsbakken, J.I.; Peters, G.P.; Canadell, J.G.; et al. Global Carbon Budget 2018. *Earth Syst. Sci. Data* **2018**, *10*, 2141–2194. [[CrossRef](#)]

2. Stocker, T.; Qin, D.; Plattner, G.; Tignor, M.; Allen, S.; Boschung, J.; Nauels, A.; Xia, Y.; Bex, B.; Midgley, B. IPCC, 2013: Climate Change 2013: The Physical Science Basis. In *Contribution of Working Group I to the Fifth Assessment Report of the Intergovernmental Panel on Climate Change*; Cambridge University Press: Cambridge, UK, 2013.
3. Fortunat, J.; Renato, S. Rates of change in natural and anthropogenic radiative forcing over the past 20,000 years. *Proc. Natl. Acad. Sci. USA* **2008**, *105*, 1425–1430.
4. Dlugokencky, E.; Tans, P. Trends in Atmospheric Carbon Dioxide, National Oceanic & Atmospheric Administration, Earth System Research Laboratory (NOAA/ESRL). Available online: <http://www.esrl.noaa.gov/gmd/ccgg/trends/global.html> (accessed on 19 October 2019).
5. Le Quéré, C.; Moriarty, R.; Andrew, R.M.; Canadell, J.G.; Sitch, S.; Korsbakken, J.I.; Friedlingstein, P.; Peters, G.P.; Andres, R.J.; Boden, T.A.; et al. Global Carbon Budget 2015. *Earth Syst. Sci. Data* **2015**, *7*, 349–396. [[CrossRef](#)]
6. Randerson, J.T.; Thompson, M.V.; Conway, T.J.; Fung, I.Y.; Field, C.B. The contribution of terrestrial sources and sinks to trends in the seasonal cycle of atmospheric carbon dioxide. *Glob. Biogeochem. Cycles* **1997**, *11*, 535–560. [[CrossRef](#)]
7. He, Z.; Zeng, Z.-C.; Lei, L.; Bie, N.; Yang, S. A Data-Driven Assessment of Biosphere-Atmosphere Interaction Impact on Seasonal Cycle Patterns of XCO₂ Using GOSAT and MODIS Observations. *Remote Sens.* **2017**, *9*, 251. [[CrossRef](#)]
8. Graven, H.D.; Keeling, R.F.; Piper, S.C.; Patra, P.K.; Stephens, B.B.; Wofsy, S.C.; Welp, L.R.; Sweeney, C.; Tans, P.P.; Kelley, J.J. Enhanced Seasonal Exchange of CO₂ by Northern Ecosystems Since 1960. *Science* **2013**, *341*, 1085–1089. [[CrossRef](#)]
9. Zeng, N.; Zhao, F.; Collatz, G.J.; Kalnay, E.; Salawitch, R.J.; West, T.O.; Guanter, L. Agricultural Green Revolution as a driver of increasing atmospheric CO₂ seasonal amplitude. *Nature* **2014**, *515*, 394–397. [[CrossRef](#)]
10. Detmers, R.G.; Hasekamp, O.; Aben, I.; Houweling, S.; van Leeuwen, T.T.; Butz, A.; Landgraf, J.; Köhler, P.; Guanter, L.; Poulter, B. Anomalous carbon uptake in Australia as seen by GOSAT. *Geophys. Res. Lett.* **2015**, *42*, 8177–8184. [[CrossRef](#)]
11. He, Z.; Lei, L.; Welp, L.; Zeng, Z.-C.; Bie, N.; Yang, S.; Liu, L. Detection of Spatiotemporal Extreme Changes in Atmospheric CO₂ Concentration Based on Satellite Observations. *Remote Sens.* **2018**, *10*, 839. [[CrossRef](#)]
12. Chevallier, F.; Palmer, P.I.; Feng, L.; Boesch, H.; O'Dell, C.W.; Bousquet, P. Toward robust and consistent regional CO₂ flux estimates from in situ and spaceborne measurements of atmospheric CO₂. *Geophys. Res. Lett.* **2014**, *41*, 1065–1070. [[CrossRef](#)]
13. Deng, F.; Jones, D.B.A.; Henze, D.K.; Bousseres, N.; Bowman, K.W.; Fisher, J.B.; Nassar, R.; O'Dell, C.; Wunch, D.; Wennberg, P.O.; et al. Inferring regional sources and sinks of atmospheric CO₂ from GOSAT XCO₂ data. *Atmos. Chem. Phys.* **2014**, *14*, 3703–3727. [[CrossRef](#)]
14. Eldering, A.; Wennberg, P.O.; Crisp, D.; Schimel, D.S.; Gunson, M.R.; Chatterjee, A.; Liu, J.; Schwandner, F.M.; Sun, Y.; O'Dell, C.W. The Orbiting Carbon Observatory-2 early science investigations of regional carbon dioxide fluxes. *Science* **2017**, *358*, eaam5745. [[CrossRef](#)] [[PubMed](#)]
15. Ciais, P.; Dolman, A.J.; Bombelli, A.; Duren, R.; Peregon, A.; Rayner, P.J.; Miller, C.; Gobron, N.; Kinderman, G.; Marland, G.; et al. Current systematic carbon-cycle observations and the need for implementing a policy-relevant carbon observing system. *Biogeosciences* **2014**, *11*, 3547–3602. [[CrossRef](#)]
16. Heimann, M. Searching out the sinks. *Nat. Geosci.* **2009**, *2*, 3–4. [[CrossRef](#)]
17. Watanabe, H.; Hayashi, K.; Saeki, T.; Maksyutov, S.; Nasuno, I.; Shimono, Y.; Hirose, Y.; Takaichi, K.; Kanekon, S.; Ajiro, M.; et al. Global mapping of greenhouse gases retrieved from GOSAT Level 2 products by using a kriging method. *Int. J. Remote Sens.* **2015**, *36*, 1509–1528. [[CrossRef](#)]
18. Kathryn, M.K.; Wofsy, S.C.; Thomas, N.; Janusz, E.; Ehleringer, J.R.; Stephens, B.B. Assessment of ground-based atmospheric observations for verification of greenhouse gas emissions from an urban region. *Proc. Natl. Acad. Sci. USA* **2012**, *109*, 8423–8428.
19. Zeng, Z.-C.; Lei, L.; Strong, K.; Jones, D.B.A.; Guo, L.; Liu, M.; Deng, F.; Deutscher, N.M.; Dubey, M.K.; Griffith, D.W.T.; et al. Global land mapping of satellite-observed CO₂ total columns using spatio-temporal geostatistics. *Int. J. Digit. Earth* **2016**. [[CrossRef](#)]
20. Kataoka, F.; Crisp, D.; Taylor, T.E.; O'Dell, C.W.; Lee, R.A.M. The Cross-Calibration of Spectral Radiances and Cross-Validation of CO₂ Estimates from GOSAT and OCO-2. *Remote Sens.* **2017**, *9*, 1158. [[CrossRef](#)]

21. Heymann, J.; Reuter, M.; Hilker, M.; Buchwitz, M.; Schneising, O.; Bovensmann, H.; Burrows, J.P.; Kuze, A.; Suto, H.; Deutscher, N.M.; et al. Consistent satellite XCO₂ retrievals from SCIAMACHY and GOSAT using the BESD algorithm. *Atmos. Meas. Tech.* **2015**, *8*, 2961–2980. [[CrossRef](#)]
22. Hakkarainen, J.; Ialongo, I.; Tamminen, J. Direct space-based observations of anthropogenic CO₂ emission areas from OCO-2. *Geophys. Res. Lett.* **2016**, *43*, 11400–411406. [[CrossRef](#)]
23. Bovensmann, H.; Buchwitz, M.; Burrows, J.P.; Reuter, M. A remote sensing technique for global monitoring of power plant CO₂ emissions from space and related applications. *Atmos. Meas. Tech.* **2010**, *3*, 55–110. [[CrossRef](#)]
24. Schwandner, F.M.; Gunson, M.R.; Miller, C.E.; Carn, S.A.; Eldering, A.; Krings, T.; Verhulst, K.R.; Schimel, D.S.; Nguyen, H.M.; Crisp, D. Spaceborne detection of localized carbon dioxide sources. *Science* **2017**, *358*, eaam5782. [[CrossRef](#)] [[PubMed](#)]
25. Nassar, R.; Hill, T.G.; Mclinden, C.A.; Wunch, D.; Jones, D.B.A.; Crisp, D.; Nassar, R.; Hill, T.G.; Mclinden, C.A.; Wunch, D. Quantifying CO₂ emissions from individual power plants from space. *Geophys. Res. Lett.* **2017**, *44*, 10045–10053. [[CrossRef](#)]
26. Liu, J.; Bowman, K.W.; Schimel, D.S.; Parazoo, N.C.; Jiang, Z.; Lee, M.; Bloom, A.A.; Wunch, D.; Frankenberg, C.; Sun, Y.; et al. Contrasting carbon cycle responses of the tropical continents to the 2015–2016 El Nino. *Science* **2017**, *358*. [[CrossRef](#)]
27. Feng, L.; Palmer, P.I.; Parker, R.J.; Deutscher, N.M.; Feist, D.G.; Kivi, R.; Morino, I.; Sussmann, R. Estimates of European uptake of CO₂ inferred from GOSAT XCO₂ retrievals: Sensitivity to measurement bias inside and outside Europe. *Atmos. Chem. Phys.* **2016**, *16*, 1289–1302. [[CrossRef](#)]
28. Bovensmann, H.; Burrows, J.P.; Buchwitz, M.; Frerick, J.; Noël, S.; Rozanov, V.V.; Chance, K.V.; Goede, A.P.H. SCIAMACHY: Mission Objectives and Measurement Modes. *J. Atmos. Sci.* **1999**, *56*, 125–150. [[CrossRef](#)]
29. Yokota, T.; Yoshida, Y.; Eguchi, N.; Ota, Y.; Tanaka, T.; Watanabe, H.; Maksyutov, S. Global concentrations of CO₂ and CH₄ retrieved from GOSAT: First preliminary results. *Sci. Online Lett. Atmos.* **2009**, *5*, 160–163. [[CrossRef](#)]
30. Boesch, H.; Baker, D.; Connor, B.; Crisp, D.; Miller, C. Global Characterization of CO₂ Column Retrievals from Shortwave-Infrared Satellite Observations of the Orbiting Carbon Observatory-2 Mission. *Remote Sens.* **2011**, *3*, 270–304. [[CrossRef](#)]
31. Zeng, Z.; Lei, L.; Hou, S.; Ru, F.; Guan, X.; Zhang, B. A Regional Gap-Filling Method Based on Spatiotemporal Variogram Model of Columns. *IEEE Trans. Geosci. Remote Sens.* **2014**, *52*, 3594–3603. [[CrossRef](#)]
32. Hammerling, D.M.; Michalak, A.M.; O'Dell, C.; Kawa, S.R. Global CO₂ distributions over land from the Greenhouse Gases Observing Satellite (GOSAT). *Geophys. Res. Lett.* **2012**, *39*, 1–6. [[CrossRef](#)]
33. Hai, N.; Katzfuss, M.; Cressie, N.; Braverman, A. Spatio-Temporal Data Fusion for Very Large Remote Sensing Datasets. *Technometrics* **2014**, *56*, 174–185.
34. Liu, Y.; Wang, X.; Guo, M.; Tani, H. Mapping the FTS SWIR L2 product of XCO₂ and XCH₄ data from the GOSAT by the Kriging method—A case study in East Asia. *Int. J. Remote Sens.* **2012**, *33*, 3004–3025. [[CrossRef](#)]
35. Jing, Y.; Shi, J.; Wang, T.; Sussmann, R. Mapping global atmospheric CO₂ concentration at high spatiotemporal resolution. *Atmosphere* **2014**, *5*, 870–888. [[CrossRef](#)]
36. Tadi, J.M.; Qiu, X.; Miller, S.; Michalak, A.M. Spatio-temporal approach to moving window block kriging of satellite data. *Geosci. Model Dev.* **2017**, *10*, 1–17. [[CrossRef](#)]
37. Reuter, M.; Bovensmann, H.; Buchwitz, M.; Burrows, J.P.; Connor, B.J.; Deutscher, N.M.; Griffith, D.W.T.; Heymann, J.; Keppel-Aleks, G.; Messerschmidt, J.; et al. Retrieval of atmospheric CO₂ with enhanced accuracy and precision from SCIAMACHY: Validation with FTS measurements and comparison with model results. *J. Geophys. Res.* **2011**, *116*. [[CrossRef](#)]
38. O'Dell, C.W.; Connor, B.; Bösch, H.; O'Brien, D.; Frankenberg, C.; Castano, R.; Christi, M.; Eldering, D.; Fisher, B.; Gunson, M.; et al. The ACOS CO₂ retrieval algorithm—Part 1: Description and validation against synthetic observations. *Atmos. Meas. Tech.* **2012**, *5*, 99–121. [[CrossRef](#)]
39. Wunch, D.; Wennberg, P.O.; Osterman, G.; Fisher, B.; Naylor, B.; Roehl, C.M.; Dell, C.; Mandrake, L. Comparisons of the Orbiting Carbon Observatory-2 (OCO-2) XCO₂ measurements with TCCON. *Atmos. Meas. Tech.* **2017**, *10*, 2209–2238. [[CrossRef](#)]

40. Wunch, D.; Wennberg, P.O.; Toon, G.C.; Connor, B.J.; Fisher, B.; Osterman, G.B.; Frankenberg, C.; Mandrake, L.; O'Dell, C.; Ahonen, P.; et al. A method for evaluating bias in global measurements of CO₂ total columns from space. *Atmos. Chem. Phys.* **2011**, *11*, 12317–12337. [[CrossRef](#)]
41. Liang, A.; Gong, W.; Han, G.; Xiang, C. Comparison of Satellite-Observed XCO₂ from GOSAT, OCO-2, and Ground-Based TCCON. *Remote Sens.* **2017**, *9*, 1033. [[CrossRef](#)]
42. Peters, W.; Jacobson, A.R.; Sweeney, C.; Andrews, A.E.; Conway, T.J.; Masarie, K.; Miller, J.B.; Bruhwiler, L.M.; Petron, G.; Hirsch, A.I.; et al. An atmospheric perspective on North American carbon dioxide exchange: CarbonTracker. *Proc. Natl. Acad. Sci. USA* **2007**, *104*, 18925–18930. [[CrossRef](#)]
43. Connor, B.J.; Boesch, H.; Toon, G.; Sen, B.; Miller, C.; Crisp, D. Orbiting Carbon Observatory: Inverse method and prospective error analysis. *J. Geophys. Res. Atmos.* **2008**, *113*, 1–14. [[CrossRef](#)]
44. Rodgers, C.D.; Connor, B.J. Intercomparison of remote sounding instruments. *J. Geophys. Res. Atmos.* **2003**, *108*. [[CrossRef](#)]
45. Wang, T.; Shi, J.; Jing, Y.; Zhao, T.; Ji, D.; Xiong, C. Combining XCO₂ measurements derived from SCIAMACHY and GOSAT for potentially generating global CO₂ maps with high spatiotemporal resolution. *PLoS ONE* **2014**, *11*, e0148152. [[CrossRef](#)] [[PubMed](#)]
46. Olsen, S.C.; Randerson, J.T. Differences between surface and column atmospheric CO₂ and implications for carbon cycle research. *J. Geophys. Res. Atmos.* **2004**, *109*. [[CrossRef](#)]
47. Kevin Robert, G.; Law, R.M.; Scott, D.; Rayner, P.J.; David, B.; Philippe, B.; Lori, B.; Yu-Han, C.; Philippe, C.; Songmiao, F. Towards robust regional estimates of CO₂ sources and sinks using atmospheric transport models. *Nature* **2002**, *415*, 626–630.
48. Lindqvist, H.; O'Dell, C.W.; Basu, S.; Boesch, H.; Chevallier, F.; Deutscher, N.; Feng, L.; Fisher, B.; Hase, F.; Inoue, M.; et al. Does GOSAT capture the true seasonal cycle of carbon dioxide? *Atmos. Chem. Phys.* **2015**, *15*, 13023–13040. [[CrossRef](#)]
49. Cogan, A.J.; Boesch, H.; Parker, R.J.; Feng, L.; Palmer, P.I.; Blavier, J.F.L.; Deutscher, N.M.; Macatangay, R.; Notholt, J.; Roehl, C.; et al. Atmospheric carbon dioxide retrieved from the Greenhouse gases Observing SATellite (GOSAT): Comparison with ground-based TCCON observations and GEOS-Chem model calculations. *J. Geophys. Res. Atmos.* **2012**, *117*, 1–17. [[CrossRef](#)]
50. Kyriakidis, P.C.; Journel, A.G. Geostatistical Space–Time Models: A Review. *Math. Geol.* **1999**, *31*, 651–684. [[CrossRef](#)]
51. De Iaco, S. Space–time correlation analysis: A comparative study. *J. Appl. Stat.* **2010**, *37*, 1027–1041. [[CrossRef](#)]
52. Iaco, S.D.; Myers, D.E.; Posa, D. Space–time analysis using a general product–sum model. *Stat. Probab. Lett.* **2001**, *52*, 21–28. [[CrossRef](#)]
53. Cressie, N.; Wikle, C.K. *Statistics for Spatio-Temporal Data*; Wiley: New York, NY, USA, 2011.
54. Liu, M.; Lei, L.; Liu, D.; Zeng, Z.-C. Geostatistical Analysis of CH₄ Columns over Monsoon Asia Using Five Years of GOSAT Observations. *Remote Sens.* **2016**, *8*, 361. [[CrossRef](#)]
55. Schneising, O.; Heymann, J.; Buchwitz, M.; Reuter, M.; Bovensmann, H.; Burrows, J.P. Anthropogenic carbon dioxide source areas observed from space: Assessment of regional enhancements and trends. *Atmos. Chem. Phys.* **2013**, *13*, 2445–2454. [[CrossRef](#)]
56. Miller, C.E.; Crisp, D.; Decola, P.L.; Olsen, S.C.; Randerson, J.T.; Michalak, A.M.; Alkhaled, A.; Rayner, P.; Jacob, D.J.; Suntharalingam, P. Precision requirements for space-based XCO₂ data. *Ir. J. Psychol. Med.* **2007**, *29*, 143–145.
57. Wu, L.; aan de Brugh, J.; Meijer, Y.; Sierk, B.; Hasekamp, O.; Butz, A.; Landgraf, J. XCO₂ observations using satellite measurements with moderate spectral resolution: Investigation using GOSAT and OCO-2 measurements. *Atmos. Meas. Tech. Discuss.* **2019**, *2019*, 1–23. [[CrossRef](#)]
58. Belikov, D.A.; Bril, A.; Maksyutov, S.; Oshchepkov, S.; Saeki, T.; Takagi, H.; Yoshida, Y.; Ganshin, A.; Zhuravlev, R.; Aoki, S.; et al. Column-averaged CO₂ concentrations in the subarctic from GOSAT retrievals and NIES transport model simulations. *Polar Sci.* **2014**, *8*, 129–145. [[CrossRef](#)]

59. Kong, Y.; Chen, B.; Measho, S. Spatio-Temporal Consistency Evaluation of XCO₂ Retrievals from GOSAT and OCO-2 Based on TCCON and Model Data for Joint Utilization in Carbon Cycle Research. *Atmosphere* **2019**, *10*, 354. [[CrossRef](#)]
60. Yoshida, Y.; Kikuchi, N.; Morino, I.; Uchino, O.; Oshchepkov, S.; Bril, A.; Saeki, T.; Schutgens, N.; Toon, G.C.; Wunch, D.; et al. Improvement of the retrieval algorithm for GOSAT SWIR XCO₂ and XCH₄ and their validation using TCCON data. *Atmos. Meas. Tech.* **2013**, *6*, 1533–1547. [[CrossRef](#)]



© 2020 by the authors. Licensee MDPI, Basel, Switzerland. This article is an open access article distributed under the terms and conditions of the Creative Commons Attribution (CC BY) license (<http://creativecommons.org/licenses/by/4.0/>).